Characterization of spin relaxation anisotropy in Co using spin pumping

Yi Li,* Wei Cao, and W. E. Bailey†

Materials Science and Engineering, Department of Applied Physics and Applied Mathematics, Columbia University, New York, New York 10027, USA

(Received 12 February 2015; revised manuscript received 23 October 2016; published 23 November 2016)

Ferromagnets are believed to exhibit strongly anisotropic spin relaxation, with relaxation lengths for spin longitudinal to the magnetization significantly longer than those for spin transverse to the magnetization. Here, we characterize the anisotropy of spin relaxation in Co using the spin pumping contribution to Gilbert damping in noncollinearly magnetized $Py_{1-x}Cu_x$/Cu/Co trilayer structures. The static magnetization angle between $Py_{1-x}Cu_x$ and Co, adjusted under field bias perpendicular to film planes, controls the projections of longitudinal and transverse spin current pumped from $Py_{1-x}Cu_x$ into Co. We find nearly isotropic absorption of pure spin current in Co using this technique; fits to a diffusive transport model yield the longitudinal spin relaxation length <2 nm in Co. The longitudinal spin relaxation lengths found are an order of magnitude smaller than those determined by current-perpendicular-to-planes giant magnetoresistance measurements, but comparable with transverse spin relaxation lengths in Co determined by spin pumping.

DOI: 10.1103/PhysRevB.94.174439

I. INTRODUCTION

A key question for spin electronics concerns the relaxation mechanisms for spin current injected into a variety of materials. Spin relaxation in ferromagnets (Fs), central for spin momentum transfer, is special because of the anisotropy axis presented by the spontaneous magnetization **M** [1–8]. Longitudinal spin relaxation [1], with spin polarization σ parallel (antiparallel) to **M**, causes spin accumulation to decrease exponentially with distance over a scale greater than the electronic mean free path [2]. Transverse spin relaxation, with σ orthogonal to **M**, is governed by the dephasing process of spin-up and spin-down eigenmodes due to their different Fermi wave vectors, leading to oscillation and decay of spin accumulation on a scale shorter than the electronic mean free path [3–8]. The characteristic length scales for the two different spin relaxation processes in ferromagnets, λ_{sr}^{L} for longitudinal and λ_{sr}^{T} for transverse spin relaxation, have been evaluated largely using two separate experimental techniques: magnetotransport [9] for λ_{sr}^{L} and ferromagnetic resonance (FMR) [10,11] for λ_{sr}^{T}. These two measurements characterize charge-accompanied and chargeless spin current, respectively [1,12,13]. Estimates of λ_{sr}^{L} come from the F layer thickness dependence of current-perpendicular-to-planes giant magnetoresistance (CPP-GMR) [9,14–16]; extracted values of λ_{sr}^{L} range from 5 nm for $Ni_{79}Fe_{21}$ up to 40 nm for Co at room temperature. FMR measurements of spin pumping, for collinearly magnetized F_1/Cu/F_2 structures, show much shorter penetration depth (λ_c) for transverse spin current [10,11]. Co has the most anisotropic spin relaxation according to these separate measurements, with $\lambda_{sr}^{L}/\lambda_{sr}^{T} \sim 16$ taking $\lambda_{sr}^{T} \sim 2\lambda_c = 2.4$ nm [11,17].

In this manuscript, we demonstrate experimentally that the longitudinal spin relaxation length, in addition to the transverse spin relaxation length [11], can also be characterized using a spin pumping measurement, enabling a measurement of the anisotropy of spin relaxation in a given ferromagnetic layer. We present FMR measurements of the spin pumping contribution to Gilbert damping in noncollinearly magnetized $Py_{1-x}Cu_x$/Cu/Co multilayers (Py=$Ni_{79}Fe_{21}$). Using $Py_{1-x}Cu_x$ alloys, which have adjustably smaller saturation magnetization M_s than Co, we can change the magnetization alignment of $Py_{1-x}Cu_x$ and Co from collinear for in-plane FMR to near-orthogonal for perpendicular FMR. As the angle θ_M between $Py_{1-x}Cu_x$ and Co magnetization tends towards $\pi/2$, one component of injected spin from $Py_{1-x}Cu_x$ tends towards the longitudinal direction (Fig. 1), allowing us to probe anisotropy in spin relaxation through the linewidth of the $Py_{1-x}Cu_x$ layer [18,19]. We find, surprisingly, that spin relaxation, as measured through the spin pumping contribution to Gilbert damping, is mostly isotropic. In our Co films we estimate $\lambda_{sr}^{L} < 2$ nm for all different $Py_{1-x}Cu_x$/Cu/Co samples, which is comparable to its transverse counterpart (∼2.4 nm) but inconsistent with the much longer (∼40 nm) lengths reported from room-temperature CPP-GMR [9,16].

II. EXPERIMENT

Three types of thin-film heterostructures were prepared by UHV sputtering and characterized by FMR. Pseudo-spin-valve-type $Py_{1-x}Cu_x$(t)/Cu(5 nm)/Co(5 nm) trilayers were used to characterize the anisotropy of spin-current absorption in Co. Their response was compared with two types of $Py_{1-x}Cu_x$(t) alloy control samples. Bilayers of $Py_{1-x}Cu_x$(5 nm*)/Cu(5 nm) and trilayers of $Py_{1-x}Cu_x$(5 nm*)/Cu(5 nm)/Pt(3 nm) were used to characterize the background damping of the alloy and the spin mixing conductance of the alloy/Cu interface, respectively. Co(5 nm)/Cu(5 nm)/Pt(3 nm) is also deposited. For the alloy Cu contents $x = 0$ to 0.4 were prepared in each case, using confocal sputtering from Py and Cu targets [20]; thicker (10 nm*) alloy layers were used for $x = 0.4$. All layers were deposited on Si/SiO_2 substrates, seeded by Ta(5 nm)/Cu(5 nm) and capped by Ta(2 nm). See Ref. [21] for details on preparation.

Room temperature, variable frequency (3–26 GHz), swept-field FMR measurements were used to characterize the

*yl2600@columbia.edu
†web54@columbia.edu

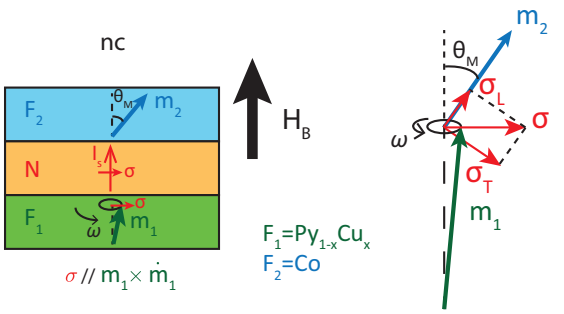

FIG. 1. (Left) Noncollinear magnetization alignment of the $F_1/N/F_2$ trilayer at the FMR condition for F_1. (Right) $\mathbf{m}_1$ is driven into precession, pumping spin current into $\mathbf{m}_2$, with spin components both longitudinal (σ_L) and transverse (σ_T) to the $\mathbf{m}_2$ magnetization.

samples, with instrumentation as described in Ref. [22]. In order to characterize the FMR relaxation of the $Py_{1-x}Cu_x$ layer under noncollinear magnetization alignment with Co, two types of measurements were carried out. First, we compare the frequency-dependent linewidths of $Py_{1-x}Cu_x$ and $Py_{1-x}Cu_x/Cu/Co$ samples in both in-plane (parallel-condition, pc) and perpendicular (normal-condition, nc) FMR [23], for a series of four measurements at a given alloy content x; see Figs. 2(c), 3, and 4. Here we expect the Co magnetization of trilayer samples to vary from fully perpendicular to the film plane at high biasing field H_B (high $\omega/2\pi$) to nearly parallel to the film plane at low H_B (low $\omega/2\pi$), while the $Py_{1-x}Cu_x$ magnetization is always perpendicular to the film plane. Second, we compare the polar angle-dependent linewidths of $Py_{0.8}Cu_{0.2}$ and $Py_{0.8}Cu_{0.2}/Cu/Co$ samples at a fixed frequency of $\omega/2\pi = 10$ GHz; see Fig. 5. Here we expect the misalignment angle θ_M to change from zero to maximum as we rotate the biasing field from in-plane (pc) to out-of-plane (nc).

III. THEORETICAL MODELING

Theoretical models for the spin pumping contribution to damping under noncollinear magnetization alignment of symmetric $F_1/N/F_1$ structures were developed in Refs. [18,19]. We have extended these models to consider asymmetric $F_1/N/F_2$ structures where $F_1 = Py_{1-x}Cu_x$ and $F_2 = Co$ in our samples. In the spin valve structure, the spin-pumping damping enhancement $\Delta\alpha_{sp}$ of F_1 is caused by the dissipation of spin current in F_2. If F_1 and F_2 are misaligned by an angle θ_M, where $\cos\theta_M = \mathbf{m}_1 \cdot \mathbf{m}_2$ (Fig. 1), during small-angle precession of F_1, the polarization of spin current pumped into F_2 will oscillate from fully transverse to maximally longitudinal. The instantaneous spin-pumping damping will then oscillate from $\alpha_{sp}(0^\circ) = \Delta\alpha_0 \times \tilde{g}_2^{\uparrow\downarrow}/(\tilde{g}_1^{\uparrow\downarrow} + \tilde{g}_2^{\uparrow\downarrow})$, as given in the standard collinear case [24], to a minimum value given by (Appendix A):

$$\Delta\alpha_{sp}(\theta_M) = \Delta\alpha_0 \frac{g_2^*(A\sin^2\theta_M - B\sin\theta_M\cos\theta_M) + \tilde{g}_2^{\uparrow\downarrow}(C\cos^2\theta_M - B\sin\theta_M\cos\theta_M)}{AC - B^2}. \quad (1)$$

Here, $\tilde{g}_i^{\uparrow\downarrow}$ and g_i^* ($i = 1, 2$) are the effective transverse and longitudinal spin conductances, respectively; $\Delta\alpha_0 = \gamma\hbar\tilde{g}_1^{\uparrow\downarrow}/(4\pi M_s t_F)$ is the damping enhancement with effective spin mixing conductance of $\tilde{g}_1^{\uparrow\downarrow}$ [22]; in Eq. (1), $A(\theta_M) = g_1^*\sin^2\theta_M + \tilde{g}_1^{\uparrow\downarrow}\cos^2\theta_M + \tilde{g}_2^{\uparrow\downarrow}$, $B(\theta_M) = (\tilde{g}_1^{\uparrow\downarrow} - g_1^*)\sin\theta_M\cos\theta_M$, and $C(\theta_M) = g_1^*\cos^2\theta_M + \tilde{g}_1^{\uparrow\downarrow}\sin^2\theta_M + g_2^*$. We take the arithmetic mean of the two extreme cases as the effective damping enhancement, as found to be valid in Ref. [19]. See Appendix A for details.

To maximize the spin pumping anisotropy at finite θ_M, we use Co (5 nm) for F_2, where the dimension is chosen to be significantly thicker than the transverse spin penetration depth, $\lambda_c = 1.2$ nm [11], and thinner than the reported longitudinal relaxation length λ_{sr}^L, ~38 nm [9], resulting in a large expected asymmetry in spin relaxation. In the analysis of relaxation in noncollinearly magnetized structures, we take spin mixing conductances $\tilde{g}_i^{\uparrow\downarrow}$ as parameter inputs, determined from the measurements on the Pt control structures, and take the longitudinal spin relaxation length λ_{sr}^L as a fit parameter.

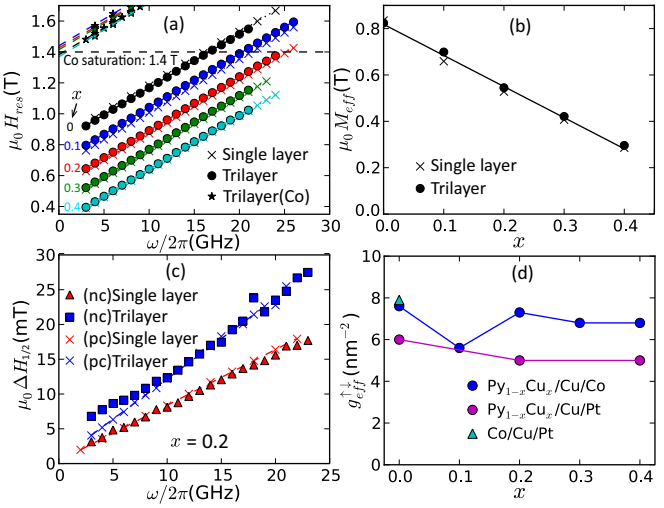

FIG. 2. (a) Perpendicular (nc-FMR) resonance field $\mu_0 H_{res}$ for $Py_{1-x}Cu_x$ single layers and $Py_{1-x}Cu_x/Cu/Co$ trilayers, $x = 0$–0.4, as a function of frequency $\omega/2\pi$. (b) Effective magnetization $\mu_0 M_{eff}$ extracted from (a) as a function of x. (c) Resonance linewidths $\mu_0\Delta H_{1/2}$ of the $Py_{0.8}Cu_{0.2}$ single layer and trilayer as a function of frequency $\omega/2\pi$. The spin pumping enhancement is clearly visible in the increased slope (α) of the trilayer data; the low-frequency deviation is discussed in Fig. 3. (d) Effective spin mixing conductances $g_{eff}^{\uparrow\downarrow}$ of $Py_{1-x}Cu_x/Cu/Co$, $Py_{1-x}Cu_x/Cu/Pt$, and $Co/Cu/Pt$.

IV. RESULTS AND ANALYSIS

Figure 2 summarizes the results of fixed-angle nc-and pc-FMR measurements for the three sample series. In Fig. 2(a), we plot resonance fields $\mu_0 H_{res}$ as a function of frequency for

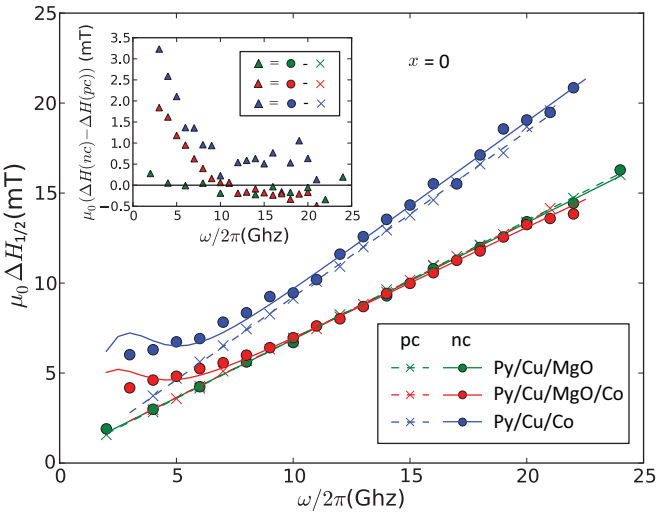

FIG. 3. pc- and nc-FMR linewidths for single (Py) and trilayer (Py/Cu/Co) structures, introducing MgO interlayers to suppress spin pumping. Dashed lines are linear fits to pc-FMR linewidths. Solid curves assume (magnetostatic) interlayer coupling of 10 mT acting on Py and reproduce the low-frequency upturn in linewidth, seen to be present equally with and without MgO. (Inset) enhancements of nc-FMR linewidth over pc-FMR linwidth for the three samples.

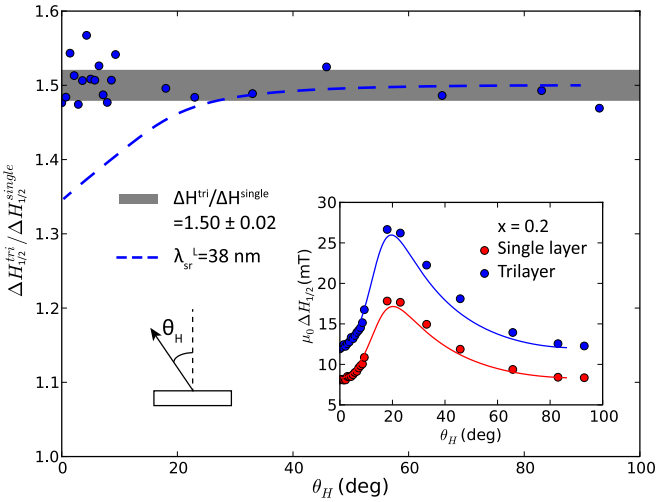

FIG. 5. Angle-dependent linewidth ratio $\Delta H^{\rm tri}_{1/2}/\Delta H^{\rm single}_{1/2}$. The shadowed region shows the average with error bar (1.50 ± 0.02). (Inset) Angular dependence of $\mu_0\Delta H_{1/2}$ for $Py_{0.8}Cu_{0.2}$ and $Py_{0.8}Cu_{0.2}$/Cu/Co at $\omega/2\pi = 10$ GHz. Solid lines are macrospin calculations.

single layers and trilayers in nc-FMR. The good agreement in the $\mu_0 H_{\rm res}$ of $Py_{1-x}Cu_x$ measured in single layers and trilayers demonstrates that $Py_{1-x}Cu_x$ properties are reproducible in deposition. In Fig. 2(b), the effective magnetizations $\mu_0 M_{\rm eff}$, extracted from fits to the linear Kittel equation $\omega/\gamma = \mu_0(H_{\rm res} - M_{\rm eff})$, are plotted as a function of x. The data show

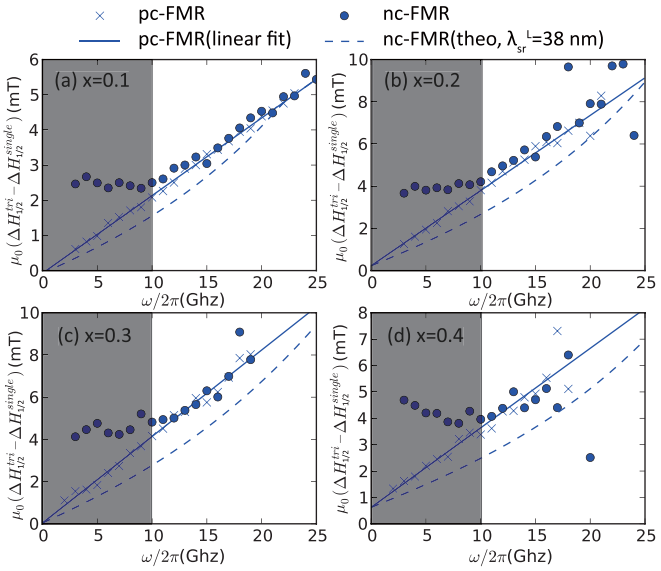

FIG. 4. Spin pumping contribution to linewidth in pc- and nc-FMR. (a)–(d) Linewidth enhancement of $Py_{1-x}Cu_x$ between single layers and trilayers in pc- and nc-FMR, $x = 0.10.4$. Solid lines are linear fits to the pc data (crosses); dashed curves are predicted from Eq. (1) using $\lambda^L_{\rm sf} = 38$ nm. The shadows at $\omega/2\pi \leqslant 10$ GHz denote where the low-frequency linewidth broadenings are significant.

Slater-Pauling dilution of magnetic moment in the $Py_{1-x}Cu_x$ layer with increasing Cu content [20].

In Fig. 2(c), we plot full-width half-maximum linewidth $\mu_0\Delta H_{1/2}$ as a function of $\omega/2\pi$ at $x = 0.2$. Gilbert-type damping, $\mu_0\Delta H_{1/2} = \mu_0\Delta H_0 + 2\alpha\omega/\gamma$, with negligible inhomogeneous broadening $\mu_0\Delta H_0$, is observed for both pc- and nc-FMR in the single layer and for pc-FMR in the trilayer. The linewidths agree closely for pc- and nc-FMR in the single layer, showing a negligible role for two-magnon scattering in the linewidth [25]. In the trilayer, nc and pc linewidths agree well for frequencies above 10 GHz. These observations hold for samples with all Cu content $0 \geqslant x \geqslant 0.4$; the deviations at low frequency are discussed in Fig. 3. The effective spin mixing conductances $g^{\uparrow\downarrow}_{\rm eff}$ of trilayer samples are extracted from $\Delta\alpha_{\rm sp} = \gamma\hbar g^{\uparrow\downarrow}_{\rm eff}/(4\pi M_s t_M)$, shown above where $\Delta\alpha_{\rm sp}$ is the difference in α between trilayers and single layers. In Fig. 2(d), we show the extracted $g^{\uparrow\downarrow}_{\rm eff}$ for $Py_{1-x}Cu_x$/Cu/Co and $Py_{1-x}Cu_x$/Cu/Pt structures as a function of x. We also plot $g^{\uparrow\downarrow}_{\rm eff}$ of Co/Cu/Pt for reference. The lower level of $g^{\uparrow\downarrow}_{\rm eff} \sim 7$ nm $^{-2}$ for $Py_{1-x}Cu_x$/Cu/Co, compared with $\sim$15 nm $^{-2}$ measured in Ref. [11], is likely to be from a more resistive Cu layer, which adds an additional resistance of $(2e^2/h)t_{\rm Cu}/\sigma_{\rm Cu}$ to the inverse of total spin mixing conductance where $\sigma_{\rm Cu}$ is the Cu conductivity. Using these $g^{\uparrow\downarrow}_{\rm eff}$ values, we extract the effective spin mixing conductance of $Py_{1-x}Cu_x$/Cu and Co/Cu interfaces, shown in Appendix B. These parameters will be used to determine the longitudinal spin relaxation lengths from the spin pumping data in Figs. 4 and 5.

In the measurements presented in Fig. 2(c), the nc-FMR linewidths are measured at applied fields below the saturation field for Co, $\mu_0 M_{\rm eff} = 1.4$ T. The saturation field corresponds to a nc-FMR resonance frequency for $Py_{0.8}Cu_{0.2}$ of 25 GHz, as shown in Fig. 2(a). With the resultant noncollinear magnetization alignment in the trilayer, we expect to see

spin-pumping damping $\Delta\alpha_{sp}$ for $Py_{0.8}Cu_{0.2}$ reduced in nc-FMR compared with the values in pc-FMR. Instead, we find that the linewidths of the trilayer measured in pc- and nc-FMR agree closely when $\omega/2\pi > 10$ GHz. Furthermore, in nc-FMR there is an additional broadening from 2–10 GHz in the trilayers which is not predicted by the model.

In order to determine whether the low-frequency broadening is related to spin pumping, we have also measured pc- and nc-FMR linewidths of Py(5 nm)/Cu(5 nm)/MgO(2 nm) and Py(5 nm)/Cu(3 nm)/MgO(2 nm)/Co(5 nm) structures, deposited with the same seed and capping layers. MgO interlayers are known to suppress spin pumping [26]. Introducing MgO between Py and Co, we show in Fig. 3 that the pc linewidths of Py in trilayer Py/Cu/Co (blue crosses) are restored to those of single-layer Py/Cu/MgO (overlapping green and red crosses), demonstrating suppression of spin pumping between Py and Co. However, we see a very similar upturn in low-frequency (<10 GHz) Py linewidth in nc-FMR (red circles), similar to that shown in Fig. 2(c). We attribute this low-frequency behavior to an interlayer coupling which cants the magnetization of Py a few degrees off the film normal when Co is not fully saturated along the film normal (i.e., $H_B < M_{eff}$). The solid curves in Fig. 3 assume a coupling field of 10 mT on Py, parallel to the local Co magnetization, which reproduce the linewidth broadening of nc-FMR. The peaklike features around 3 GHz show the maximal Gilbert damping enhancement when the Py magnetization is canted, as demonstrated in Fig. 5 inset.

Figure 4 shows the central result of the paper. We compare the spin-pumping linewidth enhancements, $\mu_0(\Delta H_{1/2}^{tri} - \Delta H_{1/2}^{single})$, between pc- and nc-FMR (crosses and circles) in Fig. 4(a)–4(d). Here, $\Delta H_{1/2}^{single}$ and $\Delta H_{1/2}^{tri}$ are the linewidths of $Py_{1-x}Cu_x$ in $Py_{1-x}Cu_x$/Cu single layers and $Py_{1-x}Cu_x$/Cu/Co trilayers, respectively. The spin pumping linewidths are quite linear as a function of frequency for the pc-FMR data, as expected. However, above 10 GHz (shaded regions), they are also quite linear in nc-FMR, which is not expected. Collinear and noncollinear spin pumping linewidths agree closely. This behavior is in contrast to the predicted behavior using $\lambda_{sr}^{L} = 38$ nm for Co, measured by CPP-GMR [9], and calculated in dashed curves according to the theory in Appendix A. From the evident agreement between pc- and nc-linewidths above 10 GHz, for all Cu content x, we find no evidence for anisotropy in spin relaxation in our Co films. Best fits to the data yield longitudinal spin relaxation lengths $\lambda_{sr}^{L} < 2$ nm in each of the four cases, approximately equal to the previously measured transverse length $\lambda_{sr}^{T} = 2.4$ nm [11].

Our model has assumed single-domain (macrospin) behavior in both Co and $Py_{1-x}Cu_x$ layers. For $Py_{1-x}Cu_x$ under field bias well in excess of M_s, the magnetization is well saturated, but for the Co layer, with higher M_s, nonuniform magnetization is possible. For greater control over the Co domain state, we have also carried out angle-dependent, fixed-frequency FMR measurements on $Py_{0.8}Cu_{0.2}$ and $Py_{0.8}Cu_{0.2}$/Cu/Co. Here the Co layer can be saturated more easily because the biasing field is canted away from the normal condition. The frequency is set to 10 GHz, where the low-frequency linewidth broadening of $Py_{0.8}Cu_{0.2}$ is insignificant (Figs. 3 and 4). As the field angle θ_H goes from 90° to 0° (pc to nc), the angle between the magnetizations of $Py_{0.8}Cu_{0.2}$ and Co changes from zero to maximum noncollinearity (~50°) and $\Delta\alpha_{sp}$ would be expected to decrease significantly where the spin relaxation length in Co is marketly anisotropic.

Figure 5 inset shows the angular dependence of $\Delta H_{1/2}^{single}$ (red) and $\Delta H_{1/2}^{tri}$ (blue) for $Py_{0.8}Cu_{0.2}$. The data can be reproduced through a macrospin model[12,27] as shown in the solid curves, using similar magnetizations and *isotropic* dampings extracted from Fig. 2(a) and (c) ($\mu_0 M_{eff} = 0.53$ T, $\alpha_1 = 0.0114$ for the single layer, $\mu_0 M_{eff} = 0.55$ T, $\alpha_3 = 0.0168$ for the trilayer). The inhomogeneous broadenings are negligible, shown in Fig. 2(c). For small enough θ_H, the resonance field of the Co starts to fall below the expected macrospin value (Appendix C). We take the angle at which this behavior appears (at $\theta_H \sim 18°$) to be the limit above which we have the greatest confidence in single-domain ordering of Co.

In the main panel of Fig. 5, we replot the trilayer and single-layer linewidths for $Py_{0.8}Cu_{0.2}$, shown in the inset, as the ratio $\Delta H_{1/2}^{tri}/\Delta H_{1/2}^{single}$. Because the inhomogeneous linewidths are negligble for the structures (<0.5 mT), the linewidth ratio for *isotropic* spin pumping would be approximated well through the ratio of the Gilbert damping for the two configurations, $\Delta H_{1/2}^{tri}/\Delta H_{1/2}^{single} = 1 + \Delta\alpha_{sp}/\alpha_1$. We find that the linewidth ratio is in fact constant within experimental error. The blue curve shows the expected behavior for anisotropic spin relaxation, assuming $\lambda_{sr}^{L} = 38$ nm, with a marked decrease in the linewidth ratio for low angles θ_H. A best fit to these data returns $\lambda_{sr}^{L} < 1.1$ nm. If we restrict our attention to field angles $\theta_H \geqslant 18°$, above which we have confidence in macrospin behavior of the Co layer, the best fit is not changed greatly, with $\lambda_{sr}^{L} \leqslant 4$ nm, within experimental error of the transverse length λ_{sr}^{T}.

V. DISCUSSIONS

Extrinsic effects, i.e., issues of sample quality, may play some role in the results. First, longitudinal spin relaxation lengths λ_{sr}^{L}, if equated with the spin diffusion length λ_{sd}, are inversely proportional to (defect-related) resistivity [28]. However, four-point probe measurements of the resistivity of our Co (5 nm) films show 25 $\mu\Omega\cdot$cm, comparable with the 18 $\mu\Omega\cdot$cm reported in the room-temperature CPP-GMR experiment [9], and therefore comparably long spin diffusion lengths should be expected. Second, we see that the spin mixing conductances $g_{eff}^{\uparrow\downarrow}$ of $Py_{1-x}Cu_x$/Cu/Co measured here are lower than those measured in Ref. [11], on structures deposited elsewhere. The most plausible source of the reduction is a more resistive Cu layer, which adds an additional resistive term [29,30] $(2e^2/h)t_{Cu}\rho_{Cu}$ to $g_{eff}^{\uparrow\downarrow}$. Here, however, the bulk Cu properties should have little influence over either spin relaxation length and should not affect the anisotropy of spin relaxation strongly.

It is possible that pure (chargeless) spin current and spin polarized (charged) current relax differently, and with different length scales, in ferromagnetic metals. Our estimate of λ_{sr}^{L} in Co is consistent with a general observation that spin relaxation as measured in spin pumping/FMR is shorter-ranged than it is as measured in magnetotransport. For Pd and Pt, spin pumping measures relaxation lengths of 1–5 nm [11,31–33] and

CPP-GMR magnetotransport measures spin diffusion lengths of 10–20 nm [34,35]. Secondly, the clear evidence of spin pumping into ferrimagnetic insulators such as YIG [36–38] shows that relaxation mechanisms unrelated to electron transport in the FM, e.g., interfacial exchange-mediated magnon excitations [39], must also be relevant in those materials. The latter mechanism seems to require zero characteristic length in the ferromagnet and is a possible source for the short-ranged longitudinal spin relaxation.

A second possibility, mentioned in a review of CPP-GMR experiments (see Sec. 2.2.2 in Ref. [16]), is that the long spin diffusion length of Co has not been measured accurately in the past due to technical issues of the CPP-GMR measurement. Our finding of nearly isotropic spin relaxations in Co, in this scenario, may alternately imply that the short spin diffusion length observed in Py is not far away from that of Co.

VI. CONCLUSIONS

In summary, we have experimentally demonstrated that the spin relaxation in Co, as measured by noncollinear spin pumping, is largely isotropic. The estimated longitudinal spin relaxation length, <2 nm, is an order of magnitude smaller than measured by magnetotransport but comparable to the transverse spin relaxation length.

ACKNOWLEDGMENT

We acknowledge NSF-DMR-1411160 for support.

APPENDIX A: CALCULATION OF SPIN-PUMPING DAMPING FOR NONCOLLINEARLY MAGNETIZED, ASYMMETRIC TRILAYERS

Consider an asymmetric ferromagnet/noble-metal/ferromagnet ($F_1/N/F_2$) spin-valve trilayer structure, shown in Fig. 6(a). The time-averaged magnetization of F_1 is pictured along the film-normal, although it can take any angle with respect to the film-normal. We assume that F_1 undergoes small-angle precession. F_2 is noncollinearly magnetized with respect to F_1, where θ is the angle of noncollinearity or misalignment; $\theta = 0$ for $\mathbf{m}_1 \parallel \mathbf{m}_2$, where $\mathbf{m}_i$, $i = 1$ or 2, is the unit vector of the magnetization $\mathbf{M}_i$ of F_i. The magnetizaton of F_2 is taken to be stationary. The spin current flows from the N spacer to each of the F layers F_1, F_2 are [10,18,19,24]

$$\mathbf{I}_s^{\mathrm{N}\to\mathrm{F}_i} = \frac{g_i^*}{4\pi}\mathbf{m}_i(\boldsymbol{\mu}_{sN}\cdot\mathbf{m}_i) + \frac{\tilde{g}_i^{\uparrow\downarrow}}{4\pi}\mathbf{m}_i\times\boldsymbol{\mu}_{sN}\times\mathbf{m}_i, \quad \text{(A1)}$$

where $\boldsymbol{\mu}_{sN}$ is the spin accumulation vector in the N layer, g_i^* and $\tilde{g}_i^{\uparrow\downarrow}$ are the effective longitudinal spin conductance and transverse spin mixing conductance for F_i/N interface, respectively. Here, the spin current vector denotes the direction of spin polarization, the direction of current flow always being normal to interfaces. The conservation of spin angular momentum, assuming spin-current conservation (negligible dissipation) N, gives

$$\mathbf{I}_s^{\mathrm{N}\to\mathrm{F}_1} + \mathbf{I}_s^{\mathrm{N}\to\mathrm{F}_2} = \mathbf{I}_{s1}^{\mathrm{pump}}, \quad \text{(A2)}$$

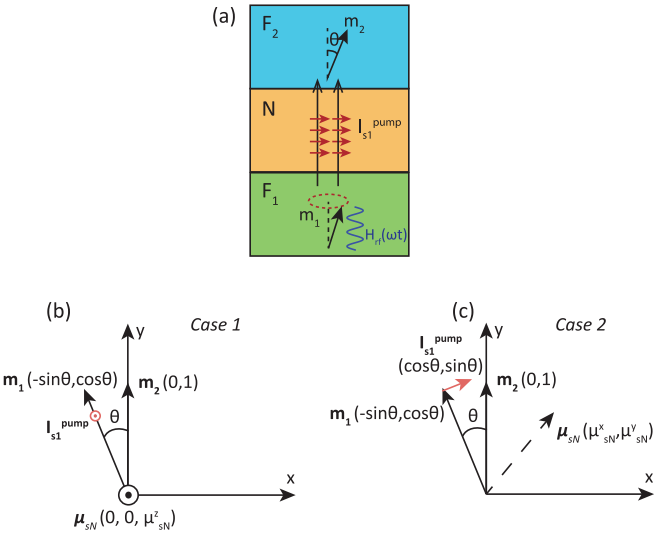

FIG. 6. (a) Magnetization configuration of the asymmetric $F_1/N/F_2$ trilayer. (b) An instant in which the spin polarization of $\mathbf{I}_{s1}^{\mathrm{pump}}$ is orthogonal to both $\mathbf{m}_1$ and $\mathbf{m}_2$. $\boldsymbol{\mu}_{sN}$ is also orthogonal to $\mathbf{m}_1$ and $\mathbf{m}_2$. (c) An instant in which the spin polarization of $\boldsymbol{I}_{s1}^{\mathrm{pump}}$ is in the same plane of $\mathbf{m}_1$ and $\mathbf{m}_2$. $\boldsymbol{\mu}_{sN}$ is also in the same plane of $\mathbf{m}_1$ and $\mathbf{m}_2$.

where $\mathbf{I}_{s1}^{\mathrm{pump}}$ is the pumped spin current from F_1 into N [13,24]:

$$\mathbf{I}_{s1}^{\mathrm{pump}} = \frac{\hbar}{4\pi}\tilde{g}_1^{\uparrow\downarrow}\mathbf{m}_1\times\dot{\mathbf{m}}_1. \quad \text{(A3)}$$

Substituting Eqs. (A1) and (A3) into the continuity expression (A2), we obtain a vector equation in terms of the vector spin accumulation $\boldsymbol{\mu}_{sN}$. To calculate the spin pumping damping enhancement, we seek solutions for $\boldsymbol{\mu}_{sN}$ in order to find the spin current flow into F_2, which is then fully relaxed and a torque is applied on F_1.

The vector $\mathbf{I}_{s1}^{\mathrm{pump}}$, proportional to $\mathbf{m}_1\times\dot{\mathbf{m}}_1$, rotates in the plane with normal given by $\mathbf{m}_1$. Assuming a finite misalignment angle θ between $\mathbf{m}_1$ and $\mathbf{m}_2$, $\mathbf{I}_{s1}^{\mathrm{pump}}$ will oscillate between fully orthogonal to $\mathbf{m}_2$ [Fig. 6(b)] and canted away from orthogonality by θ [Fig. 6(c)]. We consider these two extreme cases during the precession of $\mathbf{m}_1$:

Case 1. $\mathbf{I}_{s1}^{\mathrm{pump}} \perp \mathbf{m}_1$ and $\mathbf{I}_{s1}^{\mathrm{pump}} \perp \mathbf{m}_2$

In the situation [Fig. 6(b)], $\mathbf{I}_s^{\mathrm{N}\to\mathrm{F}_1}$, $\mathbf{I}_s^{\mathrm{N}\to\mathrm{F}_2}$, and $\boldsymbol{\mu}_{sN}$ are all parallel to $\mathbf{I}_{s1}^{\mathrm{pump}}$. In Eq. (A1), the first terms become zero and only the second terms remain. The solution of Eqs. (A1) and (A2) has a scalar form along the direction $\hat{z}$ orthogonal to both F_1 and F_2:

$$I_{s,z}^{\mathrm{N}\to\mathrm{F}_1\{\mathrm{F}_2\}} = \left(\frac{\tilde{g}_{1\{2\}}^{\uparrow\downarrow}}{\tilde{g}_1^{\uparrow\downarrow}+\tilde{g}_2^{\uparrow\downarrow}}\right)I_{s1}^{\mathrm{pump}}, \quad \text{(A4a)}$$

$$\mu_{sN}^z = \left(\frac{4\pi}{\tilde{g}_1^{\uparrow\downarrow}+\tilde{g}_2^{\uparrow\downarrow}}\right)I_{s1}^{\mathrm{pump}}. \quad \text{(A4b)}$$

It has been shown previously that [13,24] the dissipation of spin angular momentum due to a transverse spin mixing conductance $g^{\uparrow\downarrow}$ leads to an additional Gilbert damping term $\Delta\alpha = \gamma\hbar g^{\uparrow\downarrow}/4\pi M_s t_F$. With only $\mathbf{I}_s^{\mathrm{N}\to\mathrm{F}_2}$ dissipated, the

spin-pumping damping enhancement can be expressed as

$$\Delta\alpha_{sp} = I_{s2}^{\text{back}} \cdot \frac{\Delta\alpha_0}{I_{s1}^{\text{pump}}} = \Delta\alpha_0 \cdot \frac{\tilde{g}_2^{\uparrow\downarrow}}{\tilde{g}_1^{\uparrow\downarrow} + \tilde{g}_2^{\uparrow\downarrow}} \tag{A5}$$

with $\Delta\alpha_0 = \gamma\hbar\tilde{g}_1^{\uparrow\downarrow}/4\pi M_{s1}t_{F1}$. Equation (A5) is identical to the collinear spin pumping case with an effective spin mixing conductance $(\tilde{g}_{\text{eff}}^{\uparrow\downarrow})^{-1} = (\tilde{g}_1^{\uparrow\downarrow})^{-1} + (\tilde{g}_2^{\uparrow\downarrow})^{-1}$.

Case 2. $\mathbf{I}_{s1}^{\text{pump}} \parallel \mathbf{m}_1$ and $\mathbf{I}_{s1}^{\text{pump}} \parallel \mathbf{m}_2$

In this case [Fig. 6(c)], $\mathbf{I}_{s1}^{\text{pump}}$ has the largest longitudinal component along $\mathbf{m}_2$ and $\boldsymbol{\mu}_{sN}$ has only a component coplanar with $\mathbf{m}_1$ and $\mathbf{m}_2$ (μ_{sN}^x and μ_{sN}^y). In Eq. (A1), both terms need to be considered. The $\hat{x}$ and $\hat{y}$ components of Eq. (A2) can be written as

$$\begin{aligned} 4\pi I_{s1}^{\text{pump}}\begin{pmatrix}\cos\theta\\ \sin\theta\end{pmatrix} &= g_1^*(-\mu_{sN}^x\sin\theta + \mu_{sN}^y\cos\theta)\begin{pmatrix}-\sin\theta\\ \cos\theta\end{pmatrix} \\ &+ \tilde{g}_1^{\uparrow\downarrow}(\mu_{sN}^x\cos\theta + \mu_{sN}^y\sin\theta)\begin{pmatrix}\cos\theta\\ \sin\theta\end{pmatrix} \\ &+ g_2^*\mu_{sN}^y\begin{pmatrix}0\\ 1\end{pmatrix} + \tilde{g}_2^{\uparrow\downarrow}\mu_{sN}^x\begin{pmatrix}1\\ 0\end{pmatrix}. \end{aligned} \tag{A6}$$

The solution of Eq. (A6) can be expressed as

$$\mu_{sN}^x = \frac{4\pi I_{s1}^{\text{pump}}(C\cos\theta - B\sin\theta)}{AC - B^2}, \tag{A7a}$$

$$\mu_{sN}^y = \frac{4\pi I_{s1}^{\text{pump}}(A\sin\theta - B\cos\theta)}{AC - B^2}, \tag{A7b}$$

where

$$A(\theta) = g_1^*\sin^2\theta + \tilde{g}_1^{\uparrow\downarrow}\cos^2\theta + \tilde{g}_2^{\uparrow\downarrow}, \tag{A8a}$$

$$B(\theta) = (\tilde{g}_1^{\uparrow\downarrow} - g_1^*)\sin\theta\cos\theta, \tag{A8b}$$

$$C(\theta) = g_1^*\cos^2\theta + \tilde{g}_1^{\uparrow\downarrow}\sin^2\theta + g_2^*. \tag{A8c}$$

The spin torque is equal to the component of $\mathbf{I}_s^{\text{N}\to\text{F}_2}$ transverse to $\mathbf{m}_1$, or the component which is parallel to $\mathbf{I}_{s1}^{\text{pump}}$. Thus the spin-pumping damping enhancement can be written in terms of the defined misalignment-dependent quantities $A(\theta)$, $B(\theta)$, and $C(\theta)$ as

$$\Delta\alpha_{sp}(\theta) = \frac{\mathbf{I}_s^{\text{N}\to\text{F}_2}\cdot\mathbf{I}_{s1}^{\text{pump}}}{I_{s1}^{\text{pump}}}\cdot\frac{\Delta\alpha_0}{I_{s1}^{\text{pump}}} = \Delta\alpha_0\cdot\frac{g_2^*(A\sin^2\theta - B\sin\theta\cos\theta) + \tilde{g}_2^{\uparrow\downarrow}(C\cos^2\theta - B\sin\theta\cos\theta)}{AC - B^2}. \tag{A9}$$

Equation (A9) recovers Eq. (1) in the main text. It is easy to verify that at $\theta = 0^\circ$ Eq. (A9) recovers Eq. (A5), same as the collinear spin pumping.

Having treated the two special spin current orientations, we need to take the average of all the orientation possibilities. We refer to the calculation by Taniguchi *et al.* [19], that in a symmetric spin valve ($\text{F}_1 = \text{F}_2$) the small-precession limit of averaged spin-pumping damping enhancement is equal to the arithmetic mean of damping enhancement with out-of-plane $\mathbf{I}_{s1}^{\text{pump}}$ (case 1) and in-plane $\mathbf{I}_{s1}^{\text{pump}}$ (case 2). The Eq. (13) in Ref. [19] can be simplified, at small precession angle, as

$$\Delta\alpha_{sp} = \Delta\alpha_0\left[1 - \frac{(\nu/2)\sin^2\theta}{1 - \nu^2\cos^2\theta}\right], \tag{A10}$$

which is the average of $\Delta\alpha_0$ and $\Delta\alpha_0[1 - \nu\sin^2\theta/(1 - \nu^2\cos^2\theta)]$ (Eq. (5) in Ref. [19]). We apply it to the asymmetric spin valve condition: all the theoretical curves in the main text are calculated from the mean of Eqs. (A5) and (A9). The theoretical curves in Figs. 4 and 5 of the main text are calculated using the routine, assuming $\lambda_{sr}^L = 38$ nm for Co. The new estimation of λ_{sr}^L (<2 nm) in the manuscript takes the best value that fits the damping calculation to the experimental data.

APPENDIX B: VALUES OF g^* AND $\tilde{g}^{\uparrow\downarrow}$

In this appendix, we calculate the value of the two effective spin conductances. The transverse spin mixing conductance $\tilde{g}^{\uparrow\downarrow}$ (Sharvin correction included [24]) of each interface can be calculated from the effective spin mixing conductance of $\text{Py}_{1-x}\text{Cu}_x$/Cu/Co structures and the comparison measurements of $\text{Py}_{1-x}\text{Cu}_x$/Cu/Pt and Co/Cu/Pt (Table I). For $\text{Py}_{1-x}\text{Cu}_x$/Cu/Co, the total spin mixing conductance can be expressed as

$$\frac{1}{g_{\text{Py}_{1-x}\text{Cu}_x/\text{Cu/Co}}^{\uparrow\downarrow}} = \frac{1}{\tilde{g}_{\text{Py}_{1-x}\text{Cu}_x/\text{Cu}}^{\uparrow\downarrow}} + \frac{1}{\tilde{g}_{\text{Co/Cu}}^{\uparrow\downarrow}}. \tag{B1}$$

For F/Cu/Pt (F=$\text{Py}_{1-x}\text{Cu}_x$ or Co), the effective spin mixing conductance can be formulated as

$$\frac{1}{g_{\text{F/Cu/Pt}}^{\uparrow\downarrow}} = \frac{1}{\tilde{g}_{\text{F/Cu}}^{\uparrow\downarrow}} + \frac{1}{\tilde{g}_{\text{Cu/Pt}}^{\uparrow\downarrow}}. \tag{B2}$$

In the experiment, the thicknesses of Pt are kept the same and we can treat $\tilde{g}_{\text{Cu/Pt}}^{\uparrow\downarrow}$ as a constant. Solving Eqs. (B1) and (B2), we obtain

$$\frac{1}{\tilde{g}_{\text{Py}_{1-x}\text{Cu}_x/\text{Cu}}^{\uparrow\downarrow}} = \frac{1}{g_{\text{Py}_{1-x}\text{Cu}_x/\text{Cu/Co}}^{\uparrow\downarrow}} + \frac{1}{g_{\text{Py}_{1-x}\text{Cu}_x/\text{Cu/Pt}}^{\uparrow\downarrow}} - \frac{1}{g_{\text{Co/Cu/Pt}}^{\uparrow\downarrow}}, \tag{B3a}$$

$$\frac{1}{\tilde{g}_{\text{Co/Cu}}^{\uparrow\downarrow}} = \frac{1}{g_{\text{Py}_{1-x}\text{Cu}_x/\text{Cu/Co}}^{\uparrow\downarrow}} - \frac{1}{g_{\text{Py}_{1-x}\text{Cu}_x/\text{Cu/Pt}}^{\uparrow\downarrow}} + \frac{1}{g_{\text{Co/Cu/Pt}}^{\uparrow\downarrow}}. \tag{B3b}$$

TABLE I. Experimental values of (effective) spin mixing conductance of $\text{Py}_{1-x}\text{Cu}_x$/Cu/Co, $\text{Py}_{1-x}\text{Cu}_x$/Cu/Pt, and Co/Cu/Pt samples, extracted from spin-pumping linewidth enhancements.

(Unit: nm $^{-2}$)	$x = 0$	$x = 0.1$	$x = 0.2$	$x = 0.3$	$x = 0.4$
$g_{\text{Py}_{1-x}\text{Cu}_x/\text{Cu/Co}}^{\uparrow\downarrow}$	7.6	5.6	7.3	6.8	6.8
$g_{\text{Py}_{1-x}\text{Cu}_x/\text{Cu/Pt}}^{\uparrow\downarrow}$	6.0		5.0		5.0
$g_{\text{Co/Cu/Pt}}^{\uparrow\downarrow}$	7.9				

In Table II, we list the calculated values of $\tilde{g}^{\uparrow\downarrow}_{\mathrm{Py}_{1-x}\mathrm{Cu}_x/\mathrm{Cu}}$ and $\tilde{g}^{\uparrow\downarrow}_{\mathrm{Co/Cu}}$. For $x = 0.1$ and 0.3, we take the linear interpolated values to evaluate $g^{\uparrow\downarrow}_{\mathrm{Py}_{1-x}\mathrm{Cu}_x/\mathrm{Cu/Pt}}$. In addition, we also show the values compensating the Sharvin correction, with $1/g_i^{\uparrow\downarrow} = 1/\tilde{g}_i^{\uparrow\downarrow} + 1/2g^{\mathrm{Sh}}_{\mathrm{Cu}}$, $g^{\mathrm{Sh}}_{\mathrm{Cu}} = 15\ \mathrm{nm}^{-2}$.

Compared with previous measurements [11,30], we find smaller values of $g^{\uparrow\downarrow}_{\mathrm{Py}_{1-x}\mathrm{Cu}_x/\mathrm{Cu/Co}}$ and $g^{\uparrow\downarrow}_{\mathrm{Py}_{1-x}\mathrm{Cu}_x/\mathrm{Cu}}$ for $x = 0$. However, we argue that the spin mixing conductances of Co/Cu/Pt in Table I and Co/Cu interfaces in Table II are reasonable, which ensures a good Co/Cu interface crucial for the study of spin relaxation anisotropy. It is also possible that a resistive Cu spacer contributes an additional resistance, $(2e^2/h)t_{\mathrm{Cu}}\rho_{\mathrm{Cu}}$ [24], to the right side of Eq. (B2). To reduce the spin mixing conductance of Py/Cu/Co from 15.0 nm^{-2} in Ref. [11] to 7.6 nm^{-2} in Table I, one needs to take $\rho_{\mathrm{Cu}} = 16.8\ \mu\Omega\,\mathrm{cm}$. However, we point out that this resistive scattering will contribute to both transverse and longitudinal spin conductance by the same amount, and the anisotropy of spin relaxation should not be affected. In practice, we take the effective interfacial spin mixing conductance into the model for the estimation of λ^L_{sr} and and use the values of λ^T_{sr} from Ref. [11].

The effective longitudinal spin conductance g^* can be expressed as [18]

$$\frac{1}{g^*} = \frac{g^{\uparrow\uparrow} + g^{\downarrow\downarrow}}{2g^{\uparrow\uparrow}g^{\downarrow\downarrow}} + \frac{1}{g_{sd}\tanh\left(t_F/\lambda^L_{sr}\right)}. \tag{B4}$$

In the first term, $g_i^{\uparrow\uparrow\{\downarrow\downarrow\}}$ is the interfacial spin-up (spin-down) conductance. $g^{\uparrow\uparrow\{\downarrow\downarrow\}}$ can be calculated by $1/g^{\uparrow\uparrow\{\downarrow\downarrow\}} = (e^2/h)AR^{\uparrow\{\downarrow\}}_{\mathrm{F/N}}$, where $AR^{\uparrow\{\downarrow\}}_{\mathrm{F/N}}$ is the electron interface resistance. We use the experimental value from GMR measurements: $2AR^* = (AR^{\uparrow} + AR^{\downarrow})/2 = 1.04\ \mathrm{f}\,\Omega\cdot\mathrm{m}^2$ for Co/Cu [40] and $1.0\ \mathrm{f}\Omega\cdot\mathrm{m}^2$ for Py/Cu [14]. We can calculate that $2g^{\uparrow\uparrow}g^{\downarrow\downarrow}/(g^{\uparrow\uparrow} + g^{\downarrow\downarrow}) = 26\ \mathrm{nm}^{-2}$ for both interfaces.

In the second term, g_{sd} has been expressed in Ref. [18] as

$$g_{sd} = \frac{h}{e^2\lambda^L_{sr}}\frac{2\sigma^{\uparrow}\sigma^{\downarrow}}{\sigma^{\uparrow} + \sigma^{\downarrow}}, \tag{B5}$$

where $\sigma^{\uparrow,\downarrow}$ are the spin-up/down electron conductivity in F, h is the Planck constant and e is the electronic charge. Here we simply take $\sigma^{\uparrow} = \sigma^{\downarrow} = \sigma/2$ (σ is the total electrical conductivity), which has also been done in Eq. (74) of Ref. [24]. Following this treatment, the term $2\sigma^{\uparrow}\sigma^{\downarrow}/(\sigma^{\uparrow} + \sigma^{\downarrow})$ is replaced by $\sigma/2$. Taking $\rho_{\mathrm{Co}} = 25\ \mu\Omega\,\mathrm{cm}$ and $\rho_{\mathrm{Py}} = 30\ \mu\Omega\,\mathrm{cm}$ from our four-point probe measurements and $\lambda^L_{sr} = 38$ nm for Co [9] and 4.3 nm for Py [15] from the literatures, we calculate $g_{sd}\tanh(t_F/\lambda^L_{sr})$ to be 0.18 nm^{-2} for Co and 8.3 nm^{-2} for Py when the F thickness is 5 nm; the large disagreement comes from the expected difference in λ^L_{sr}. As a result, $g^* = 0.18$ nm^{-2} for Co and 6.2 nm^{-2} for Py are obtained from Eq. (B4) and used to produce the theoretical curves in the manuscript.

In the experiment, we do not find the anisotropic response of spin pumping predicted above. According to our model, the lack of anisotropic response can be explained best through a difference in the longitudinal spin conductance g^* for Co/Cu, as this is the most dominant term in Eq. (A9) and sensitive to λ^L_{sr}. This is because in the experiments, we choose the thickness of Co to be much less than 38 nm in order to examine the spin relaxation anisotropy.

From Py to $\mathrm{Py}_{1-x}\mathrm{Cu}_x$, we should expect that both $g^{\uparrow\uparrow\{\downarrow\downarrow\}}$ and $\sigma^{\uparrow\{\downarrow\}}$ will increase due to a better conducting ability of Cu than Py. λ^L_{sr} may also vary. However, we emphasize that in Eq. (A9), the anisotropy is dominated by g_2^* and $\tilde{g}_2^{\uparrow\downarrow}$ and not sensitive to g_1^*. For example in the angular dependence of linewidth ration for $x = 0.2$ (Fig. 5 of the main text), increasing $g^*_{\mathrm{Py}_{0.8}\mathrm{Cu}_{0.2}/\mathrm{Cu}}$ by a factor of two will change the single-domain estimation of λ^L_{sr} from 1.8 ± 2.7 nm ($\leqslant 4$ nm in the main text) to 2.1 ± 2.8 nm, still much smaller than the GMR measurements. Thus for simplicity we keep using the value of g^* of Py for $\mathrm{Py}_{1-x}\mathrm{Cu}_x$ layers.

TABLE II. "$\tilde{g}_i^{\uparrow\downarrow}$": Sharvin-corrected spin mixing conductance of $\mathrm{Py}_{1-x}\mathrm{Cu}_x/\mathrm{Cu}$ and Co/Cu interfaces, calculated from Eq. (B3). "$g_i^{\uparrow\downarrow}$": interfacial spin mixing conductance compensating the Sharvin conductance of Cu layer. $i = \mathrm{Py}_{1-x}\mathrm{Cu}_x/\mathrm{Cu}$ or Co/Cu.

(Unit: nm^{-2})	$x = 0$	$x = 0.1$	$x = 0.2$	$x = 0.3$	$x = 0.4$
$\tilde{g}^{\uparrow\downarrow}_{\mathrm{Py}_{1-x}\mathrm{Cu}_x/\mathrm{Cu}}$	11.7	8.6	9.5	9.1	9.1
$\tilde{g}^{\uparrow\downarrow}_{\mathrm{Co/Cu}}$	21.9	16.2	31.5	27.2	27.2
$g^{\uparrow\downarrow}_{\mathrm{Py}_{1-x}\mathrm{Cu}_x/\mathrm{Cu}}$	8.4	6.7	7.2	7.0	7.0
$g^{\uparrow\downarrow}_{\mathrm{Co/Cu}}$	12.7	10.5	15.4	14.3	14.3

APPENDIX C: SINGLE-DOMAIN LIMIT DETERMINATION

To determine whether the Co layer is in a single-domain state in $\mathrm{Py}_{0.8}\mathrm{Cu}_{0.2}/\mathrm{Cu/Co}$ when the $\mathrm{Py}_{0.8}\mathrm{Cu}_{0.2}$ layer is at resonance, we have measured the FMR signal of Co at different θ_H. First we measure the FMR signal of $\mathrm{Py}_{0.8}\mathrm{Cu}_{0.2}$ at one angle and determine the resonance field $\mu_0 H_{\mathrm{res}}$. Next, we adjust the frequency so that the Co FMR signal can be measured at the same field. Then we compare the lineshape with the macrospin model prediction [12]. In Fig. 7(a), when $\theta_H = 18^\circ$ the resonance field $\mu_0 H_{\mathrm{res}}$ for $\mathrm{Py}_{0.8}\mathrm{Cu}_{0.2}$ is 0.53 T at 10 GHz. For Co, the resonance field is located at 0.53 T for 14.8 GHz. The macrospin model for angle-dependent FMR shows $\omega/2\pi = 14.8$ GHz,

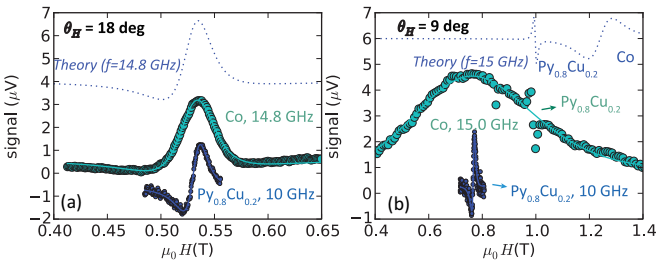

FIG. 7. Resonance peak of Co and $\mathrm{Py}_{0.8}\mathrm{Cu}_{0.2}$ independently measured in $\mathrm{Py}_{0.8}\mathrm{Cu}_{0.2}/\mathrm{Cu/Co}$ with $\theta_H = 18^\circ$ (a) and 9° (b). The resonance frequency of $\mathrm{Py}_{0.8}\mathrm{Cu}_{0.2}$ are both 10 GHz. The resonance frequency of Co is adjusted so that the $\mu_0 H_{\mathrm{res}}$ of Co is equal to $\mathrm{Py}_{0.8}\mathrm{Cu}_{0.2}$. Dashed curves show the theoretical prediction of Co resonance signals.

identical to the experiment, showing the Co can indeed be treated as a macrospin. However, for $\theta_H = 9^\circ$ [Fig. 7(b)], we find that the Co resonance is located at 15.0 GHz, quite different from the macrospin prediction of 12.3 GHz. To see the difference more clearly, we plot (dashed lines) the macrospin prediction for both $Py_{0.8}Cu_{0.2}$ and Co resonances at 15.0 GHz, based on the magnetizations and linewidths measured from perpendicular FMR. The $Py_{0.8}Cu_{0.2}$ peak matches with experiment. The calculated Co peak deviates from experiment in both resonance field and linewidth. Thus we determine the single-domain limit of θ_H to be somewhere between 9° and 18° in the sample. The upper bound 18° is used in the manuscript for the single-domain limit.

[1] T. Valet and A. Fert, Phys. Rev. B **48**, 7099 (1993).
[2] S. Zhang, P. M. Levy, and A. Fert, Phys. Rev. Lett. **88**, 236601 (2002).
[3] M. D. Stiles and A. Zangwill, Phys. Rev. B **66**, 014407 (2002).
[4] A. Shpiro, P. M. Levy, and S. Zhang, Phys. Rev. B **67**, 104430 (2003).
[5] J. Zhang and P. M. Levy, Phys. Rev. B **70**, 184442 (2004)
[6] J. Zhang, P. M. Levy, S. Zhang, and V. Antropov, Phys. Rev. Lett. **93**, 256602 (2004).
[7] J. Zhang and P. M. Levy, Phys. Rev. B **71**, 184426 (2005).
[8] C. Petitjean, D. Luc, and X. Waintal, Phys. Rev. Lett. **109**, 117204 (2012).
[9] L. Piraux, S. Dubois, A. Fert, and L. Belliard, Eur. Phys. J. B **4**, 413 (1998).
[10] T. Taniguchi, S. Yakata, H. Imamura, and Y. Ando, Appl. Phys. Express **1**, 031302 (2008).
[11] A. Ghosh, S. Auffret, U. Ebels, and W. E. Bailey, Phys. Rev. Lett. **109**, 127202 (2012).
[12] S. Mizukami, Y. Ando, and T. Miyazaki, Phys. Rev. B **66**, 104413 (2002).
[13] Y. Tserkovnyak, A. Brataas, and G. E. W. Bauer, Phys. Rev. Lett. **88**, 117601 (2002).
[14] S. D. Steenwyk, S. Y. Hsu, R. Loloee, J. Bass and W. P. Pratt, Jr., J. Magn. Magn. Mater. **170**, L1 (1997).
[15] S. Dubois, L. Piraux, J. M. George, K. Ounadjela, J. L. Duvail, and A. Fert, Phys. Rev. B **60**, 477 (1999).
[16] J. Bass and W. P. Pratt, Jr., J. Phys.: Condens. Matter **19**, 183201 (2007).
[17] J. Foros, G. Woltersdorf, B. Heinrich, and A. Brataas, J. Appl. Phys. **97**, 10A714 (2005).
[18] Y. Tserkovnyak, A. Brataas, and G. E. W. Bauer, Phys. Rev. B **67**, 140404(R) (2003).
[19] T. Taniguchi and H. ImamuraPhys. Rev. B **76**, 092402 (2007).
[20] Y. Guan and W. E. Bailey, J. Appl. Phys. **101**, 09D104 (2007).
[21] C. Cheng, N. Sturcken, K. Shepard, and W. E. Bailey, Rev. Sci. Instrum. **83**, 063903 (2012).
[22] Y. Li and W. E. Bailey, Phys. Rev. Lett. **116**, 117602 (2016).
[23] In nc-FMR, the sample normal is aligned carefully (about two axes, with <0.2° precision) to maximize $\mu_0 H_{\rm res}$ of the $Py_{1-x}Cu_x$ layers at 3 GHz. This step is critical to reduce the inhomogeneous broadening.
[24] Y. Tserkovnyak, A. Brataas, G. E. W. Bauer, and B. I. Halperin, Rev. Mod. Phys. **77**, 1375 (2005).
[25] M. J. Hurben and C. E. Patton, J. Appl. Phys. **83**, 4344 (1998).
[26] O. Mosendz, J. E. Pearson, F. Y. Fradin, S. D. Bader, and A. Hoffmann, Appl. Phys. Lett. **96**, 022502 (2010).
[27] W. Platow, A. N. Anisimov, G. L. Dunifer, M. Farle, and K. Baberschke, Phys. Rev. B **58**, 5611 (1998).
[28] J. Bass and W. P. Pratt, Jr., J. Magn. Magn. Mater. **200**, 274 (1999).
[29] M. Zwierzycki, Y. Tserkovnyak, P. J. Kelly, A. Brataas, and G. E. W. Bauer, Phys. Rev. B **71**, 064420 (2005).
[30] A. Ghosh, J. F. Sierra, S. Auffret, U. Ebels, and W. E. Bailey, Appl. Phys. Lett. **98**, 052508 (2011).
[31] W. Zhang, V. Vlaminck, J. E. Pearson, R. Divan, S. D. Bader, and A. Hoffmann, Appl. Phys. Lett. **103**, 242414 (2013).
[32] V. Vlaminck, J. E. Pearson, S. D. Bader, and A. Hoffmann, Phys. Rev. B **88**, 064414 (2013).
[33] M. Caminale, A. Ghosh, S. Auffret, U. Ebels, K. Ollefs, F. Wilhelm, A. Rogalev, and W. E. Bailey, Phys. Rev. B **94**, 014414 (2016).
[34] H. Kurt, R. Loloee, K. Eid, W. P. Pratt, Jr., and J. Bass, Appl. Phys. Lett. **81**, 4787 (2002).
[35] M. Morota, Y. Niimi, K. Ohnishi, D. H. Wei, T. Tanaka, H. Kontani, T. Kimura, and Y. Otani, Phys. Rev. B **83**, 174405 (2011).
[36] B. Heinrich, C. Burrowes, E. Montoya, B. Kardasz, E. Girt, Y.-Y. Song, Y.-Y. Sun, and M.-Z. Wu, Phys. Rev. Lett. **107**, 066604 (2011).
[37] S. M. Rezende, R. L. Rodríguez-Suárez, M. M. Soares, L. H. Vilela-Leão, D. Ley Domínguez, and A. Azevedo, Appl. Phys. Lett. **102**, 012402 (2013).
[38] R. Adur, C.-H. Du, H.-L. Wang, S. A. Manuilov, V. P. Bhallamudi, C. Zhang, D. V. Pelekhov, F.-Y. Yang, and P. C. Hammel, Phys. Rev. Lett. **113**, 176601 (2014).
[39] S. S.-L. Zhang and S. Zhang, Phys. Rev. B **86**, 214424 (2012).
[40] A. C. Reilly, W.-C. Chiang, W. Park, S. Y. Hsu, R. Loloee, S. Steenwyk, W. P. Pratt, Jr., and J. Bass, IEEE Trans. Magn. **34**, 939 (1998).